Understanding offshore high-ozone events during TRACER-AQ 2021 in Houston: Insights from WRF-CAMx photochemical modeling

Wei Li[1], Yuxuan Wang[1], Xueying Liu[1], Ehsan Soleimanian[1], Travis Griggs[1], James Flynn[1], and Paul Walter[2]

[1]Department of Earth and Atmospheric Sciences, University of Houston, Houston, Texas, USA

[2]Department of Mathematics, St. Edward's University, Austin, TX, USA

Corresponding author: Yuxuan Wang (ywang246@central.uh.edu)

Abstract. Mechanisms for high offshore ozone (O_3) events in the Houston area have not been systematically examined due to limited O_3 measurements over water. In this study, we used the datasets collected by three boats deployed in Galveston Bay and the Gulf of Mexico during the Tracking Aerosol Convection Interactions ExpeRiment/Air Quality (TRACER-AQ) field campaign period (September 2021) in combination with the Weather Research and Forecasting (WRF) coupled Comprehensive Air quality Model with Extensions (CAMx) modeling system (WRF-CAMx) to investigate the reasons for high offshore O_3. The model can capture the spatiotemporal variability of daytime (10:00-18:00) O_3 for the three boats (R > 0.7) but tends to overestimate O_3 by ~10 ppb on clean days and underestimate O_3 by ~3 ppb during high-O_3 events. The process analysis tool in CAMx identifies O_3 chemistry as the major process leading to high O_3 concentrations. The region-wide increase of long-lived VOCs through advection transits O_3 formation to be more sensitive to NO_x, leading to more O_3 production under a NOx-limited regime. In addition, the VOC-limited O_3 formation is also boosted along western Galveston Bay and the Gulf coast under high-NO_x conditions brought by the northeasterly winds from the Houston Ship Channel. Two case studies illustrate that high offshore O_3 events can develop under both large- and meso-scale circulations, indicating both the regional and local emissions need to be stringently controlled. Wind conditions are demonstrated to be important meteorological factors in such events, so they must be well represented in photochemical models to forecast air quality over the urban coastal regions accurately.

1. Introduction

The greater Houston area has been designated as ozone (O_3) nonattainment by U.S. Environmental Protection Agency (EPA) under the National Ambient Air Quality Standards (NAAQS) standards (Nonattainment Areas for Criteria Pollutants (Green Book), 2023). O_3 is a secondary criteria pollutant whose formation is non-linearly dependent on the relative abundance of its precursors: volatile organic compounds and nitrogen oxides. Houston experiences significant anthropogenic emissions of these precursors, mainly from transportation and petrochemical facilities along the Houston Ship Channel (Leuchner and Rappenglück, 2010; Soleimanian et al., 2022). In addition, due to its unique location at the land-water interface, high O_3 events in Houston are known to be related to complex

33 meteorological conditions with the interactions between synoptic and mesoscale circulations. Dry and polluted

34 continental air masses brought by northerly winds after the cold front passage are often linked with O_3 exceedances

35 (Darby, 2005; Rappenglück et al., 2008; Ngan and Byun, 2011). Extremely high O_3 can occur under a land-sea

36 breezes recirculation, in which the land breeze in the morning transports the pollution-laden air toward Galveston

37 Bay or the Gulf of Mexico, followed by the return of the aged pollutants in the afternoon by the onshore bay or sea

38 breeze (Banta et al., 2005; Caicedo et al., 2019; Li et al., 2020). Such high-O_3 events in coastal urban regions are

39 challenging for air quality models to capture as the physical and chemical processes of O_3 over both land and water

40 need to be well-constrained (Caicedo et al., 2019; Bernier et al., 2022).

41 To understand the interplay among meteorology, emissions, and chemistry, various field campaigns have been

42 deployed in the Houston area, such as the Texas Air Quality Study in 2000 and 2006 and the Deriving Information

43 on Surface Conditions from COlumn and VERtically Resolved Observations Relevant to Air Quality (DISCOVER-

44 AQ) in 2013. A common goal of these field campaigns was to evaluate the predictive ability of numerical weather

45 and air quality models using the collected observations (Misenis and Zhang, 2010; Yu et al., 2012; Li and

46 Rappenglück, 2014; Mazzuca et al., 2016; Pan et al., 2017). Although these studies greatly improve our

47 understanding of the reasons for high ozone events in Houston, they mainly focused on the onshore area due to the

48 absence of offshore measurements. Higher levels of O_3 over water bodies than the adjacent land have been observed

49 in other coastal regions with poor air quality, such as the Chesapeake Bay and Lake Michigan, due to several factors

50 including but not limited to the offshore advection of polluted air masses, photochemical productions from local

51 (e.g., marine traffic) and aged land emissions, shallow marine planetary boundary layers (PBL), the lack of NO_x

52 titration, and low dry deposition rates (Dye et al., 1995; Goldberg et al., 2014; Sullivan et al., 2019; Abdi-Oskouei et

53 al., 2022; Dreessen et al., 2023). Air quality modeling evaluations against these observations show difficulties in

54 numerical prediction of O_3 over water with an overall positive bias for low O_3 and negative bias for high O_3 due in

55 part to the misrepresentation of marine meteorology and PBL (Dreessen et al., 2019; Abdi-Oskouei et al., 2020;

56 Dacic et al., 2020; Baker et al., 2023). However, to our knowledge, high O_3 events off the Houston coast in

57 Galveston Bay and the Gulf of Mexico have not been systematically examined. The predictive ability of

58 photochemical models in capturing such events has yet to be quantified.

59 More recently, the Tracking Aerosol Convection Interactions ExpeRiment/Air Quality (TRACER-AQ) field

60 campaign revisited the Houston area in September 2021. The campaign implemented a variety of observational

61 platforms covering both offshore and onshore locations, such as stationary sites, boats, lidar, ozonesondes, and

62 airborne remote sensing. In particular, instruments onboard three boats continuously collected O_3 and

63 meteorological data from July to October over Galveston Bay and the Gulf of Mexico, which provides a valuable

64 opportunity to understand the reasons driving high O_3 concentrations over water and the O_3 non-attainment at air

65 quality monitors near the Houston coastline. Furthermore, the Texas Commission on Environmental Quality

66 (TCEQ) has created a new emission inventory for its 2019 state implementation plan (SIP) modeling platform to

67 conduct photochemical simulations using the Comprehensive Air quality Model with Extensions (CAMx) driven by

68 the Weather Research and Forecasting (WRF) meteorology. Using the established new emission inventory and

69 observations, an evaluation of offshore O_3 prediction can provide insights into model deficiencies over water and

70 help improve air quality forecasting in coastal urban regions.

71 This study aims to improve our understanding of high offshore O_3 concentrations in the Houston coastal zone during

72 the TRACER-AQ 2021 field campaign based on observations and WRF-CAMx modeling, a regulatory model used

73 by TCEQ. We first evaluate the performance of model simulations of O_3 and then investigate the reasons causing

74 high-O_3 events relative to clean days, taking advantage of the process analysis tools from CAMx. Lastly, we present

75 two case studies to better understand the development of elevated O_3 over water. Potential sources of model bias are

76 also discussed.

77 **2. Data and model setup**

78 **2.1 Meteorological and air quality observations**

79 TCEQ has O_3 and other pollutants routinely measured at the continuous ambient monitoring stations (CAMS) across

80 the Houston region. Some of these stations also observe meteorological variables, such as wind speed and direction,

81 temperature, and relative humidity (RH). These data can be downloaded from the Texas Air Monitoring Information

82 System (TAMIS, last access: 22 September 2023) website. A commercial shrimp boat and a pontoon boat owned by

83 the University of Houston (UH) were operated mainly on the east and west sides of Galveston Bay, respectively.

84 Another commercial boat, the Red Eagle, was docked to the north of Galveston Island and typically traveled up to

85 90 km offshore in the Gulf of Mexico and occasionally northward through the Ship Channel to the port of Houston.

86 Automated O_3 sampling instruments were installed on the three boats with a compact weather station measuring

87 temperature, pressure, RH, and wind conditions. The sample inlet was attached to an elevated location on the boats

88 to avoid titration from the boats' exhausts. Details of these devices can be found in Griggs et al. (submitted). In

89 addition, ozonesondes were launched from the pontoon and Red Eagle boats on selected days and locations to

90 investigate the vertical O_3 profiles. All the campaign data can be found on the TRACER-AQ website (https://www-

91 air.larc.nasa.gov/cgi-bin/ArcView/traceraq.2021, last access: 22 September 2023).

92 During the offshore operational period of July to October, hourly averaged O_3 mixing ratios exceeded 100 ppb

93 several times. We identified O_3 exceedance days when offshore boat O_3 observations registered a daily maximum 8-

94 hour average (MDA8) O_3 in exceedance of 70 ppb, the current criteria of the NAAQS for O_3. Six episodes with high

95 O_3 were obtained: July 26 – 28, August 25, September 6 – 11, September 17 – 19, September 23 – 26, and October 6

96 – 9. These episodes are accompanied by at least one CAMS site exceeding the 70 ppb MDA8 O_3 threshold,

97 indicating an extensive land-water air mass interaction.

98 **2.2 WRF and CAMx model configuration**

99 This study used the WRF model v3.9.1.1. We set up three domains with different horizontal resolutions that cover

100 the contiguous United States, Southeast Texas, and the Houston-Galveston-Brazoria region, referred to as domains

101 d01, d02, and d03, respectively, as shown in Figure 1. The corresponding horizontal resolutions and grid numbers

102 for d01 – d03 are 12 km × 12 km (373 × 310 grids), 4 km × 4 km (190 × 133 grids), and 1.33 km × 1.33 km (172 ×

103 184 grids), respectively. All domains have identical vertical resolutions with 50 hybrid sigma-eta vertical levels

104 spanning from the surface to 10 hPa. Boundary conditions of the two inner domains were generated from the outer

105 domain.

106 To select the WRF configurations that best represent the monitoring data, we designed eight model experiments with

107 different initial and boundary condition (IC/BC) inputs, microphysics options, PBL schemes, data assimilation

108 method (e.g., observation nudging), and reinitializing techniques. Details of the design and evaluation of each

109 experiment can be found in Liu et al. (2023). Based on the campaign-wide evaluation of the modeled meteorology,

110 the best simulation was used to drive the CAMx model. The model configuration of the best simulation includes the

111 hourly High-Resolution Rapid Refresh (HRRR) meteorological data as IC/BC inputs, the local closure Mellor-

112 Yamada-Nakanishi-Niino (MYNN) PBL option (Nakanishi and Niino, 2009), and the Morrison double moment

113 (2M) microphysics scheme (Morrison et al., 2009) with no nudging and reinitializing techniques applied. Other

114 settings used for the WRF simulation include the Monin-Obukhov Similarity surface layer (Foken, 2006), the Noah

115 land surface scheme (Chen and Dudhia, 2001), the Rapid Radiative Transfer Model (RRTM) longwave and

116 shortwave radiation schemes (Iacono et al., 2008), and the New Tiedtke cumulus parameterization (Zhang et al.,

117 2011).
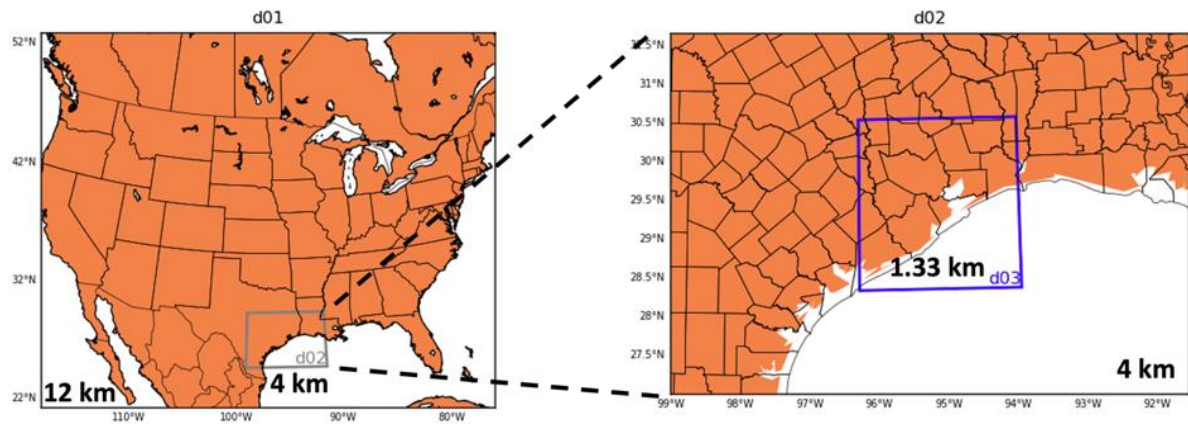
119 **Figure 1. WRF nested modeling domains and horizontal resolutions.**

121 This study also used the CAMx model v7.10. The three CAMx domains aligned with the WRF grids but had smaller

122 spatial coverage. The corresponding horizontal resolutions and grid numbers for domains 1–3 are 12 km × 12 km

123 (372 × 244 grids), 4 km × 4 km (156 × 126 grids), and 1.33 km × 1.33 km (153 × 162 grids), respectively. All

124 domains have identical vertical resolutions with 30 vertical levels from the surface to ~100 hPa. The IC/BC inputs

125 for the outmost domain are from the GEOS-Chem (v12.2.1) global simulation with NEI 2011 nitrogen oxides (NO_x)

126 emissions scaled down to 2021. The Carbon Bond version 6 revision 5 (CB6r5) was used for gas-phase chemistry,

127   including the inorganic iodine depletion of O_3 over oceanic water (Burkholder et al., 2019). The first-order eddy

128   viscosity (K-theory) diffusion scheme was selected for vertical mixing within the PBL, in which the vertical

129   diffusion coefficients (Kv) were supplied from WRF outputs. Dry deposition is based on the Wesely scheme

130   (Wesely, 1989).

131   Emission files with 12 km and 4 km spatial resolutions from the preliminary 2019 SIP modeling platform provided

132   by TCEQ are used in the simulation. These emissions include anthropogenic emissions, biogenic emissions

133   generated from the Biogenic Emission Inventory System (BEIS), wildfire emissions based on the Fire INventory

134   from NCAR (FINNv2), ship emissions estimated from the Gulfwide Emissions Inventory (GWEI). No lighting

135   emissions are included in the model. Since our domains are smaller than those in the SIP modeling, the original

136   emission files were cropped to match the grid boundaries for CAMx to read properly. In addition, we redistributed

137   the on-road emissions from 4 km to 1.33 km over the Houston area. The 4 km emission fluxes were first

138   disaggregated evenly to the 1.33 km grids and then collected onto major roads using a 1 km rasterized road shapefile

139   to produce on-major-road 1.33 km emissions. Some 1.33 km grid points off the major roads had missing values,

140   which were filled using a smoothing method that averaged eight nearby grid points. The scaling factors for on- and

141   off-major-road emissions were kept in order to maintain the on-road emission budget consistent before and after the

142   spatial redistribution. Finally, total emissions were calculated by adding the 1.33 km on- and off-major-road

143   emissions. The emissions for other sectors were also similarly interpolated to 1.33 km without separating into no- or

144   off-major-road temporary emissions. The redistributed emissions were tested to perform better in capturing the on-

145   road distributions than using the Flexi-nesting function in CAMx (Figure S1 and Table S1), which can regrid the

146   emissions on the fly.

147   The simulation was performed for two periods, July 20 – 30 and August 20 – October 13, to cover the six high-O_3

148   episodes defined in Section 2.1. A 10-day spin-up before each period was applied. Other days in the two periods are

149   considered clean scenarios with low O_3 concentrations. Process analysis, including integrated process rate analysis

150   (IPR), integrated reaction rate analysis (IRR), and chemical process analysis (CPA), was turned on when running the

151   model. IPR contains O_3 change rate from several chemical and physical processes, such as chemistry (CHEM),

152   horizontal and vertical advection (ADV) and diffusion (DIF), and deposition (DEP). IRR provides detailed

153   information about the reaction rate of all the chemical reactions in the CB6r5 scheme. CPA improves upon IRR by

154   computing parameters useful for understanding O_3 chemistry, such as O_3 production rate and regime. The abundance

155   and reactivity of ozone precursors determine the ozone production regime, which can be indicated by the loss of

156   HO_x radicals (HO_x=OH+HO2) as the termination of ozone chain reactions. Under low NOx conditions, the most

157   important HO_x loss is the self-reaction of hydroperoxyl radical (HO_2), producing hydrogen peroxide (H_2O_2), which

158   is used to represent NO_x-limited ozone production. In urban areas with high NO_x concentrations, the dominant sink

159   for HO_x radicals is the oxidation of nitrogen dioxide (NO_2) by hydroxyl radical (OH), resulting in the production of

160   nitric acid (HNO_3). Thus, the O_3 formation regime in the model is determined based on the ratio of H_2O_2 production

161   rate from HO_2 self-reaction to HNO_3 production rate from OH reaction with NO_2, in which $P(H_2O_2)/P(HNO_3) <$

162 0.35 indicates a VOC-limited regime and ≥ 0.35 indicates a NOx-limited regime (Sillman, 1995). There is no

163 transition scheme available in this method.

3. Results

3.1 Evaluation of O₃ simulations

166 The time series of the daytime (10:00 – 18:00) mean O$_3$ at the three boats are shown in Figure 2a, and the evaluation

167 statistics are listed in Table 1. The evaluation excludes nighttime data to reduce the effects from land as the boats

168 stayed at the dock at night. Indeed, an hourly time series evaluation with nighttime data included (Figure S2 and

169 Table S2) shows a larger bias between modeled ozone and boat observations. The spatiotemporal variability of

170 daytime O$_3$ at the three boats is well captured by the model with a correlation coefficient (R) value greater than 0.70.

171 Overall, the model overestimates daytime O$_3$ by 4.57 ppb (11%), 7.82 ppb (22%), and 4.35 ppb (9%) for the

172 pontoon boat, Red Eagle, and shrimp boat, respectively. On episode days, high O$_3$ mixing ratios can be found over

173 Galveston Bay and the Gulf of Mexico (Figure 2b). The model captures some of the variability (R=0.42 – 0.51),

174 with negative mean bias (MB) values of ~4.5 ppb (8%) for the pontoon and shrimp boats and a nearly unbiased

175 simulation (MB=0.05 ppb) for the Red Eagle boat. While the O$_3$ variability is better predicted on clean days (R=0.69

176 – 0.76), the model shows higher values of MB than those on high-O$_3$ days ranging from 9.15 ppb (29%) to 11.28

177 ppb (41%), which drives the overall model overestimation.
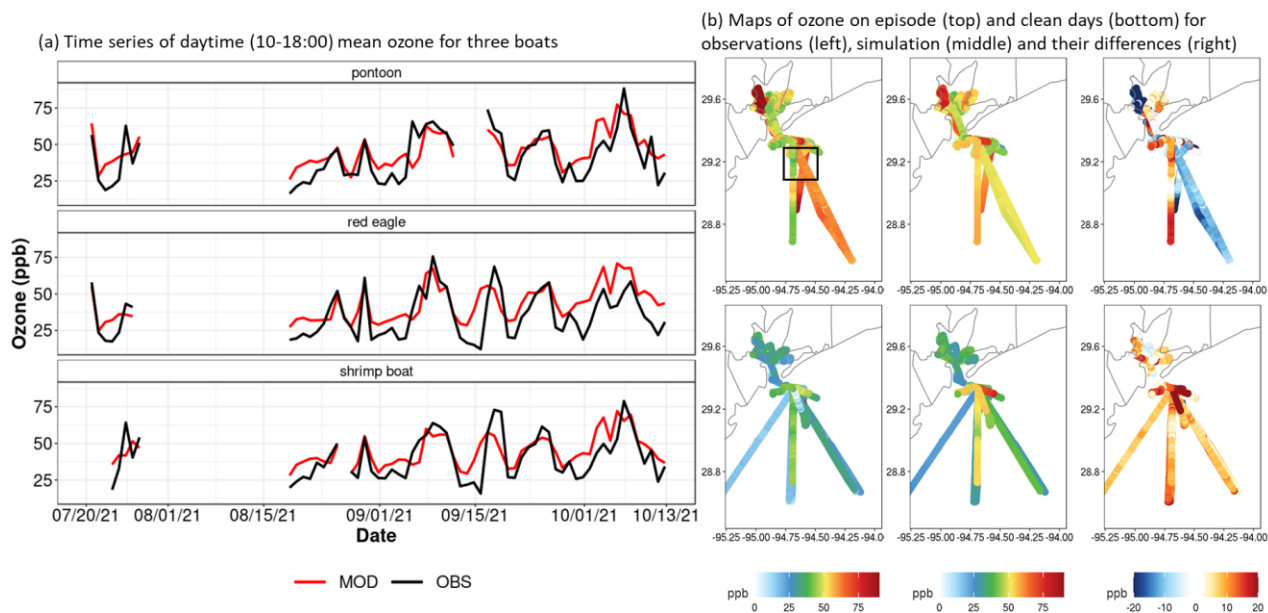
178

179 **Figure 2. (a) Time series of daytime (10:00 – 18:00) mean ozone for observations at three boats (black) and simulations**
180 **(red). (b) Maps of observed (left column), simulated (middle column), and their difference (right column) of ozone during**
181 **ozone episodes (top row) and clean days (bottom row). The black box shows the selected offshore region for process analysis**
182 **in the next section.**

183

While we did not find any previous efforts modeling offshore O_3 in the Houston area to compare our results, an evaluation against onshore measurements can help validate our model performance. The time series of the daytime mean O_3 from simulations and observations from CAMS sites are displayed in Figure 3, and the evaluation statistics are summarized in Table 2. The model captures the onshore O_3 variability (R=0.79) with an overall overestimation of 7.89 ppb (20%), mainly due to the high positive bias of 10.93 ppb (34%) on clean days. This result is comparable with the model performance from previous studies focusing on the same area (e.g., Xiao et al., 2010; Pan et al., 2015; Kommalapati et al., 2016), which further verifies the reliability of our model settings.

Table 1. Daytime (10:00 – 18:00) ozone evaluation metrics at three boats, including the observed and simulated mean values, correlation coefficient (R), mean bias (MB), normalized mean bias (MB), mean absolute error (MAE), and root mean square error (RMSE).

Boat	Period	Observed mean (ppb)	Simulated mean (ppb)	R	MB (ppb)	NMB (%)	MAE (ppb)	RMSE (ppb)
pontoon	all days	41.18	45.76	0.77	4.57	11.12	9.75	11.57
	ozone episode	58.57	54.21	0.51	-4.36	-7.44	8.34	11.31
	clean days	32.06	41.33	0.76	9.27	28.93	10.50	11.71
Red Eagle	all days	34.86	42.69	0.71	7.82	22.45	11.15	13.42
	ozone episode	51.20	51.25	0.42	0.05	0.08	9.71	11.92
	clean days	27.60	38.88	0.69	11.28	40.89	11.80	14.03
shrimp boat	all days	39.99	44.35	0.73	4.35	10.89	9.15	11.47
	ozone episode	57.22	52.22	0.43	-5.00	-8.74	8.88	11.65
	clean days	31.17	40.32	0.69	9.15	29.36	9.28	11.38

196
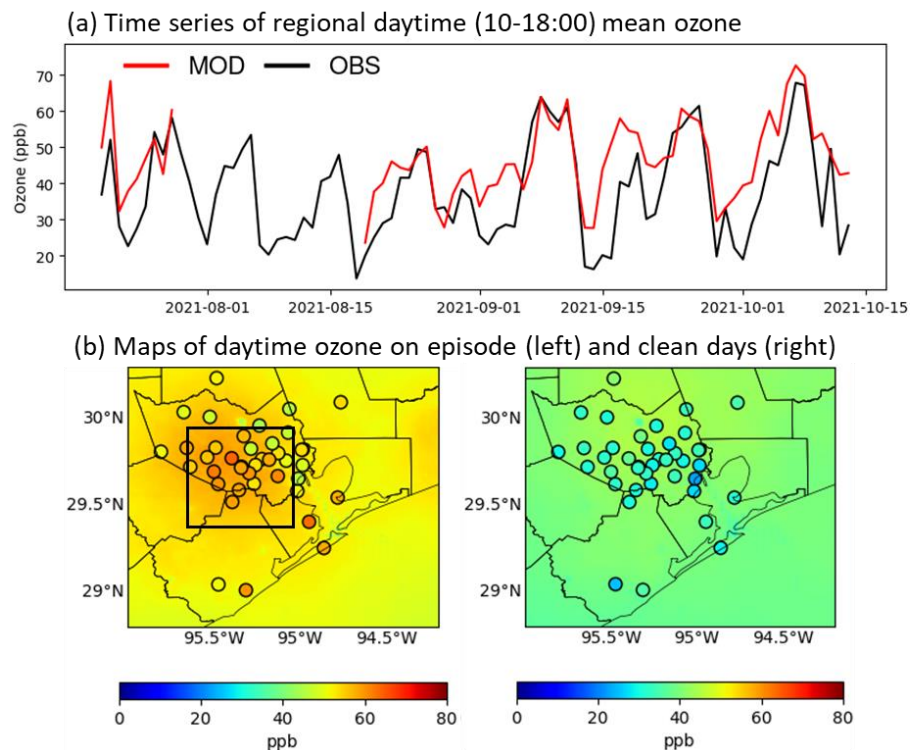
Figure 3. (a) Time series of daytime (10:00 – 18:00) mean ozone for observations at CAMS sites (OBS; black line) and simulations (MOD; red line). (b) Maps of observed (points) and simulated (background) daytime ozone during ozone episodes (left) and clean days. The black box shows the selected onshore region for process analysis in the next section.

200

201   **Table 2. Daytime (10:00 – 18:00) ozone evaluation metrics at CAMS sites. The metrics are the same as in Table 1.**

Sites	Period	Observed mean (ppb)	Simulated mean (ppb)	R	MB (ppb)	NMB (%)	MAE (ppb)	RMSE (ppb)
CAMS	all days	38.87	46.76	0.79	7.89	20.32	9.41	11.72
	ozone episode	54.63	56.17	0.64	1.54	2.81	5.31	7.15
	clean days	31.34	42.28	0.64	10.93	34.88	11.35	13.37

202

203
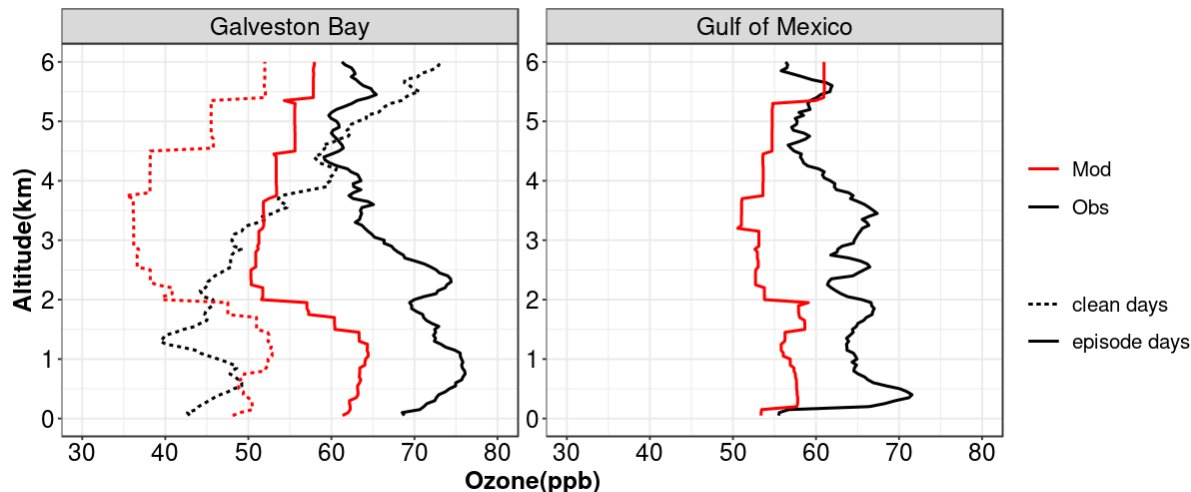
Figure 4. Ozone vertical distribution from the afternoon (12:00-18:00) ozonesonde launches (Obs; black lines) and simulations (Mod; red lines) at Galveston Bay averaged on clean days (dashed lines) and ozone-episode days (solid lines). The Gulf of Mexico only sampled ozone on high-ozone days.

We also evaluated the modeled vertical O_3 profiles against the afternoon (12:00-18:00) ozonesondes launched over Galveston Bay and the Gulf of Mexico. During the study period, there were five and nine afternoon launches over Galveston Bay on clean and O_3-episode days, respectively, while the Gulf of Mexico only had five afternoon launches during high-O_3 events. All the ozonesondes available for high-O_3 conditions are from the two episodes of September 6-11 and 23-26. The average O_3 profiles from these launches are shown in Figure 4. Free tropospheric O_3 with altitudes greater than 2 km is underestimated for both locations on both clean and O_3-episode days, which indicates the long-range transported O_3 is underrepresented by the model. Over Galveston Bay, the overestimation of O_3 within the mixed layer below 2 km on clean days changes to underestimation on episode days, and the underestimation increases from 5 ppb at the surface to 10 ppb near 1 km. The two high-O_3 episodes in September are featured by a O_3 plume between 2 – 3 km as shown by the O_3 lidar observations in Liu et al. (2023), which is missed by the model as shown by the two example days on September 9 and 24 of each episode over Galveston Bay (Figure S3). The underestimation of O_3 in the lower free troposphere and the mixed layer on episode days can be partly explained by the missing of the high-O_3 plumes which can be mixed down when the cap inversion is weak (Liu et al., 2023). There is an approximately 10 ppb underestimation across all altitudes below 4 km over the Gulf of Mexico. An ozonesonde from the Gulf of Mexico on September 9 recorded high ozone up to the top of the marine layer at 370 m, which is missed by the model and leads to the highest bias. This case will be discussed in the case study of Section 3.3.

To conclude, despite the overall model bias for vertical O_3 distributions, the acceptable model performance for offshore and onshore O_3 prediction at the surface indicates that the modeling system can be applied to conduct process analysis and help identify the processes influencing high O_3 concentrations over the water surface.

      3.2 Process analysis over the Gulf of Mexico

Figure 5. (a) Diurnal changes of simulated ozone process on clean days (stripes) and ozone-episode days (bars).

(b) Simulated ozone process changes on ozone-episode days from clean days.

228
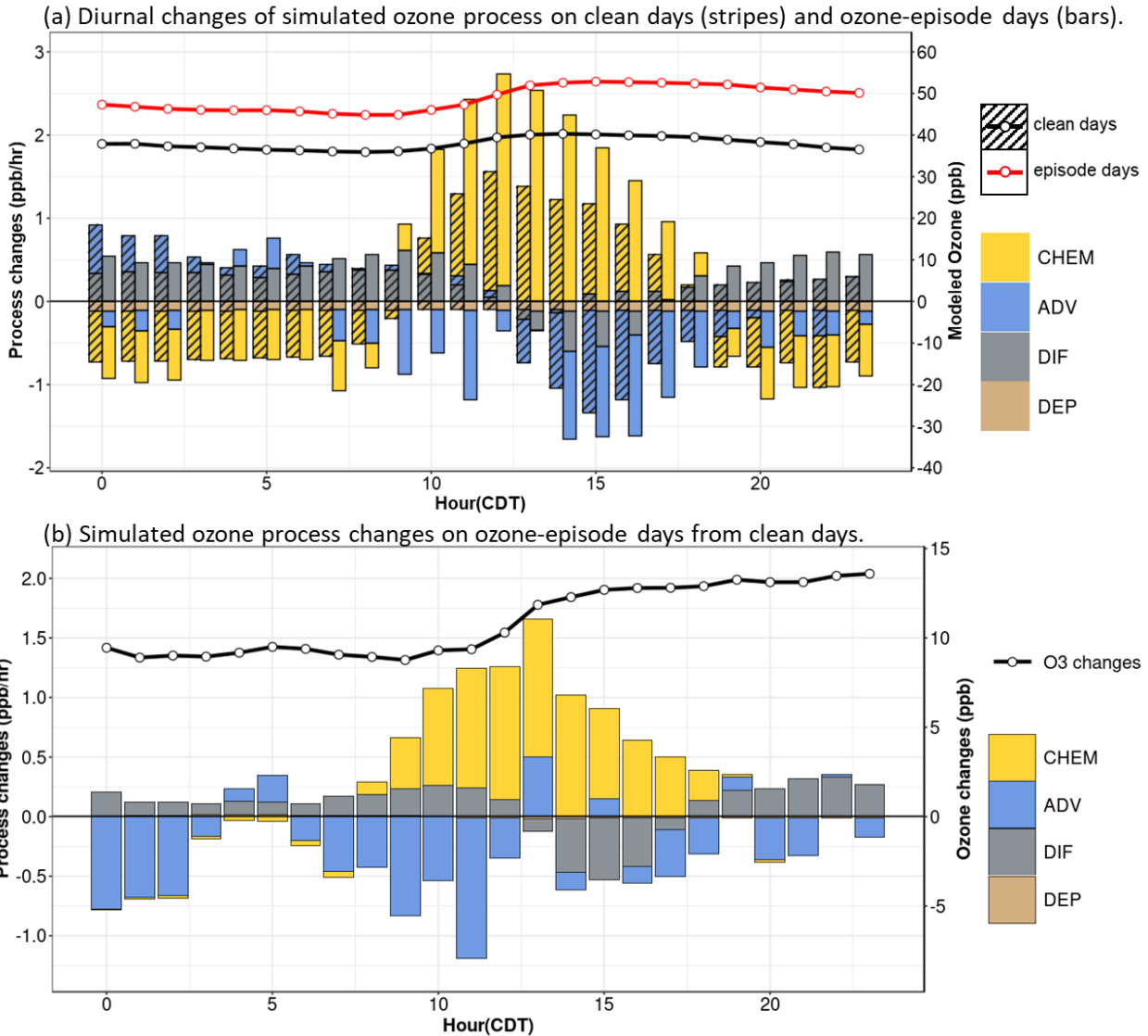
Figure 5. (a) Diurnal changes of simulated ozone processes over the Gulf of Mexico (black box in Figure 2), including chemistry (CHEM), advection (ADV), vertical diffusion (DIF), and deposition (DEP) on clean days (stripes) and O₃-episode days (bars) integrated across the lowest five model layers. Overlaid lines and points are simulated hourly ozone on clean (black) and O₃-episode (red) days. (b) Process (filled bars) and O₃ (black line) changes during high-O₃ episodes relative to clean days.

234   This section examines how the CAMx simulated O_3 processes change during high-O_3 episodes relative to clean

235   days. The process analysis is calculated over a subregion of the Gulf of Mexico with high O_3 mixing ratios observed

236   (black box in Figure 2b) and integrated across the lowest five model layers comparable to the morning PBL heights

237   over water. The diurnal average of each process on clean and O_3 episode days is shown in Figure 5a. Chemistry

238   (CHEM) is the major O_3 source during daytime and becomes the primary O_3 sink after sunset. Advection (ADV)

239   serves as a pathway for an O_3 sink for most hours, especially during the day, while vertical diffusion (DIF) mostly

240   contributes as an O_3 source. Deposition (DEP) constantly removes O_3 from the atmosphere at all hours, yet with a

241 marginal value of 0.1 ppb/hr. Similar patterns can be found over the Houston urban area with a much bigger

242 magnitude (Figure S4). During high-O_3 events, CHEM is the most important process causing higher O_3 levels over

243 water relative to clean days, followed by vertical DIF (Figure 5b). We examined the simulated O_3 vertical profiles

244 and PBL heights averaged over the process analysis region on clean and episode days in Figure S5. O_3 across the

245 entire profile is higher on episode days than clean days, indicating an elevated O_3 background on high-O_3 days. In

246 addition, the profiles of potential temperature observed by the ozonesondes show an inversion layer at ~1.5 km on

247 episode days (Figure S6). More vertical diffusion can occur if high O_3 in the inversion layer is mixed down from

248 above the PBL when the capping inversion is weak (Liu et al., 2023).

249 The CPA analysis can provide more insights into the enhanced O_3 production during high-O_3 events. We first

250 investigated the rates of HO_2 self-reaction and OH reaction with NO_2 in Figure 6a-b since they are used by the

251 model to determine the O_3 chemical regime. A region-wide increase in the HO_2 self-reaction rate leads to the

252 enhancement of PO_3 under a NO_x-limited regime (Figure 6c). Similarly, the frequency of PO_3 under a NOx-limited

253 regime also increases regionally (Figure S7). The frequency at each grid cell is the ratio of the number of hours with

254 a greater than zero NO_x-limited PO_3 to the total midday hours (11:00 – 15:00) during the study period. HO_2 is

255 formed following the oxidation of VOCs by OH. Thus, we further compared the OH reactivity of VOCs averaged

256 from 11:00 to 15:00 on clean and episode days in Figure 7. Isoprene has the highest contribution to the total VOC

257 reactivity on the land, but its reactivity does not increase during high-O_3 events. Instead, paraffin, formaldehyde, and

258 acetaldehyde are the three VOCs experiencing the highest increase of reaction rate with OH over both land by 0.22

259 ppb/hr (84%), 0.19 ppb/hr (45%) and 0.15 ppb/hr (73%) and water by 0.18 ppb/hr (114%), 0.15 ppb/hr (44%) and

260 0.11 ppb/hr (82%), respectively, which indicates a higher contribution from regional transport on episode days as

261 they are relatively long-lived VOCs capable of traveling long distances. Indeed, the paraffin IPR analysis shows that

262 the ADV process dominates the increase of paraffin during morning hours from 06:00 to 11:00 over water (Figure

263 S8). The trajectory analysis focusing on two O_3 episodes in September shows air masses were transported from the

264 northern/central states (Soleimanian et al., 2023), consistent with the wind directions demonstrated in Figure 6. Such

265 wind conditions can also bring NO_x emissions from the Houston Ship Channel downwind towards the western side

266 of Galveston Bay and the Gulf of Mexico, causing a higher OH reaction rate with NO_2 (Figure 6b) and enhanced

267 PO_3 under a VOC-limited regime (Figure 6d) therein.
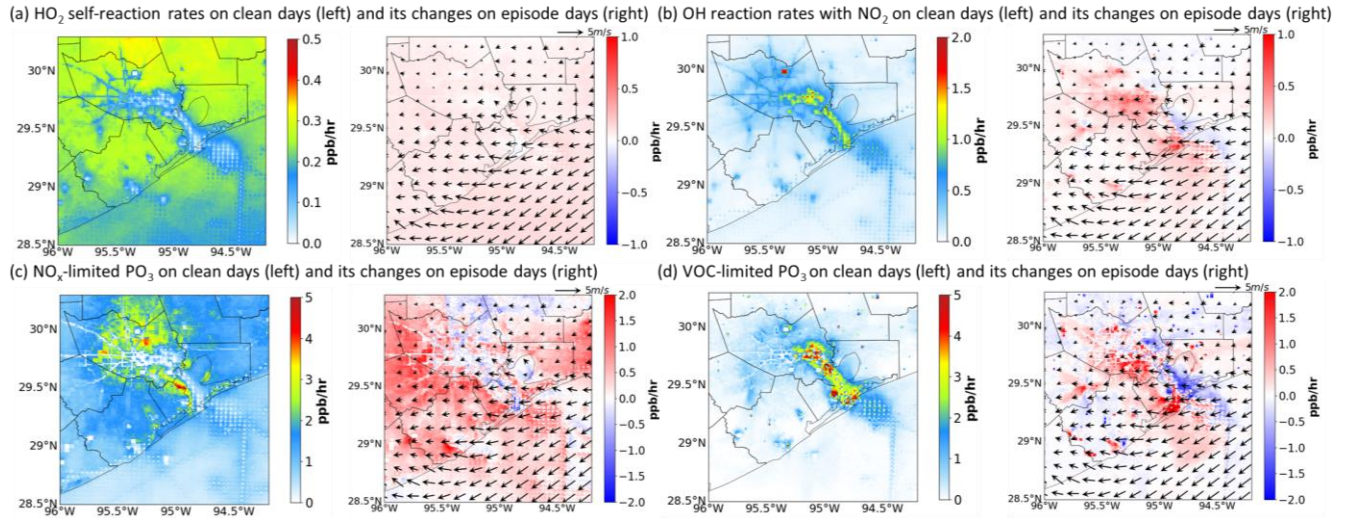
Figure 6. Maps of the rate (ppb/hr) of HO$_2$ self-reaction (a), OH reaction with NO$_2$ (b), ozone production (PO$_3$) under NO$_x$-limited (c) and VOC-limited (d) regimes on clean days (left) and its changes under episode days (right) during midday (11:00 – 15:00). Black arrows indicate the simulated wind speed and directions averaged on high-O$_3$ days.
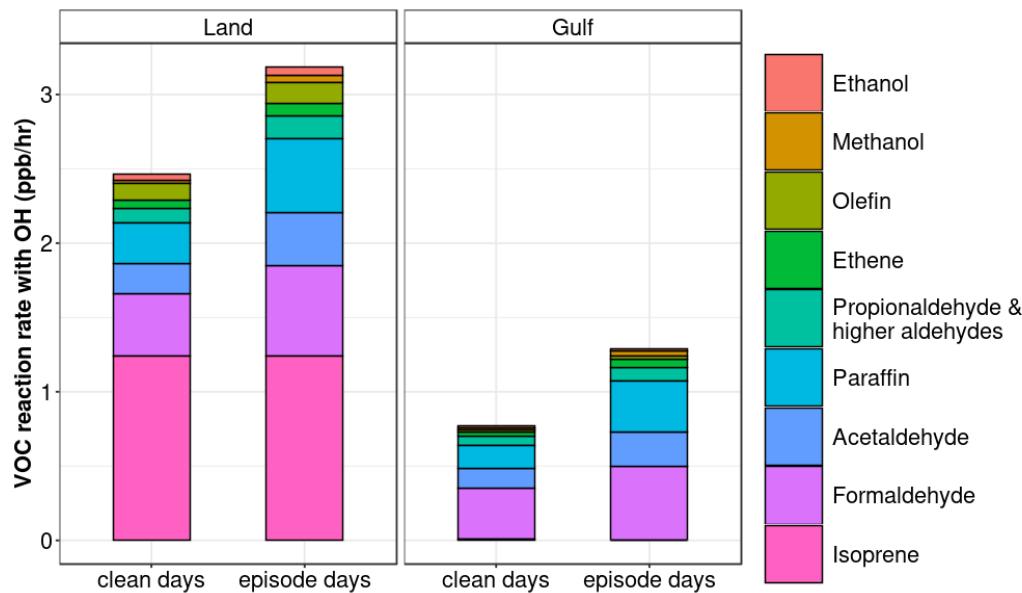
Figure 7. OH reaction rates with different VOCs on clean days and ozone-episode days during 11:00 – 15:00 over the urban area (Land; black box in Figure 3) and the Gulf of Mexico (Gulf; black box in Figure 2).

In summary, O$_3$ chemistry is the major process responsible for the high O$_3$ mixing ratios over the Gulf of Mexico during the study period. The VOC species with a long lifetime advected from the northeast increase over land and water, leading to a region-wide enhancement of PO$_3$ under a NOx-limited regime. The downwind transport of NO$_x$ from the Ship Channel also expands the VOC-limited area towards the west side of Galveston Bay and the Gulf of Mexico, contributing to the higher-than-normal PO$_3$.

280   **3.3 Case studies**

281   Although the above analysis reveals the general reasons responsible for the high offshore O₃ events, the multiple-

282   day average can miss out on some important aspects regarding the causes of these events. In this section, we selected

283   two case days, September 9 and October 7, to further demonstrate the development process of high O₃ in detail.

284   **3.3.1 Case study of September 9, 2021**
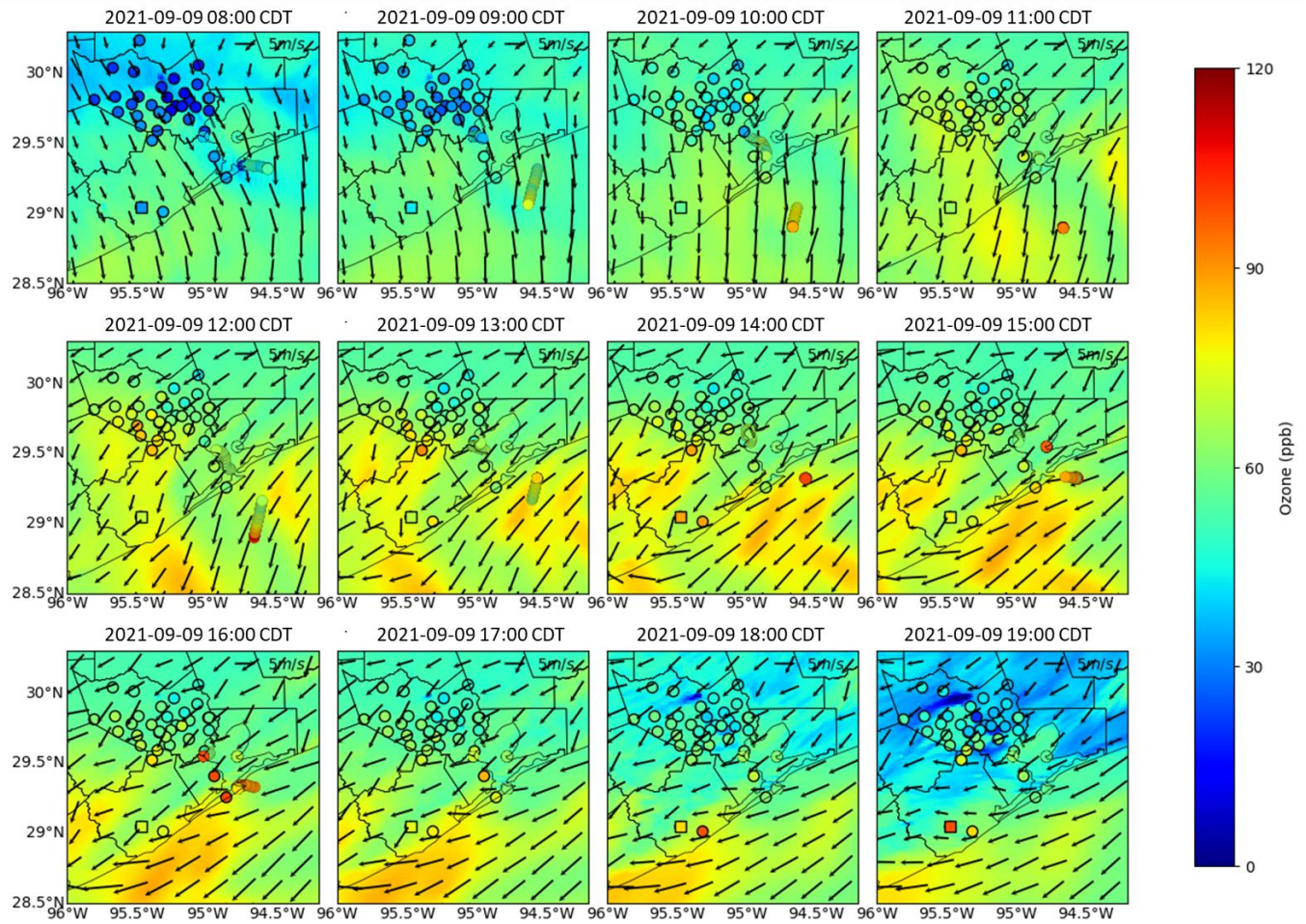
285

286   **Figure 8. Hourly simulated ozone distributions (color contours) from 08:00 to 19:00 in Central Daylight Time (CDT) on**
287   **September 9 overlaid with winds (arrows). Onshore and offshore dots indicate ozone from CAMS sites and boat**
288   **observations. The square mark highlights the Lake Jackson CAMS site.**

(a) Ozonesonde at 08:57 (CDT) [29.31⁰N, 94.56⁰W] (b) Ozonesonde at 11:45 (CDT) [28.89⁰N, 94.64⁰W] (c) Ozonesonde at 14:27 (CDT) [29.32⁰N, 94.57⁰W]

289
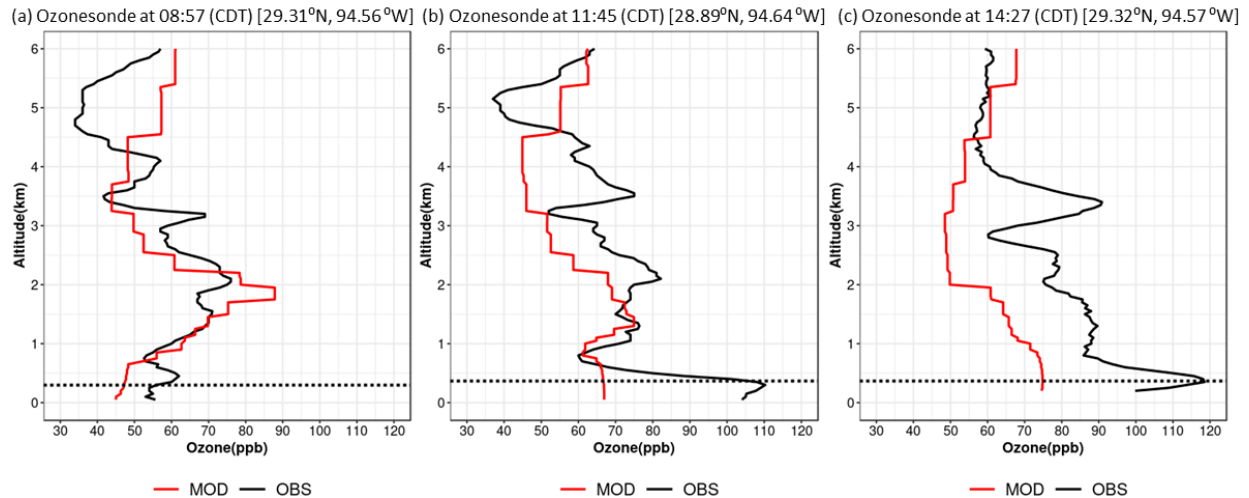
Figure 9. Ozone vertical profiles from ozonesondes (black line) and model simulations (red line) at 08:57 (a), 11:45 (b), and 14:27 (c) on September 9. Black dash lines indicate the observed boundary layer height.

Multiple CAMS sites exceeded the 70 ppb MDA8 O_3 standard on September 9, with the Red Eagle boat sampling the up to 115 ppb 1-minute O_3 in the Gulf of Mexico off the coast of Galveston Island. The hourly progression of the observed and simulated O_3 is displayed in Figure 8, overlaid with modeled winds. In the morning, the study area was dominated by northerly winds bringing the fresh emissions offshore while the pontoon boat was sampling over the west side of Galveston Bay and the Red Eagle boat was traveling in the Gulf of Mexico off the coast of Galveston Island. The ozonesonde launched near 09:00 shows a moderate level of O_3 (~55 ppb) below the shallow marine boundary layer of 200 m overlaid by a residual layer with a maximum O_3 mixing ratio of 63 ppb at ~500 m (Figure 9a). Around 11:00-12:00, with high solar radiation, the seaward-transported emissions formed O_3 through photochemical reactions over water, which was captured by the Red Eagle boat with an hourly peak O_3 mixing ratio of 92 ppb (Figure 10a). Correspondingly, the O_3 vertical profile from the 11:45 balloon launch at the Red Eagle deck recorded the highest O_3 of 110 ppb at ~315 m (Figure 9b).

However, the model missed these peak values because the simulated wind speed is up to 4 m/s higher than observations (Figure 10c), making the plume advect faster. This also leads to a two-hour earlier arrival of the modeled O_3 peak at the Lake Jackson coastal site (square mark in Figure 8) than the observed first peak at 14:00 (Figure 10a). At the same time, another plume was brought into the Gulf of Mexico from the east boundary of the domain as the wind directions changed from north to east. As the Red Eagle boat steered back to Galveston Island, all three boats sampled this plume at 14:00-17:00, resulting in the second O_3 peak at the Red Eagle boat and the only O_3 peak at the other two boats. The ozonesonde launched at 14:27 from the Red Eagle boat (Figure 9c) observed O_3 reaching 118 ppb in the plume at ~370 m. This plume was continuously transported southwestward and reached the Lake Jackson site at 19:00, producing a second O_3 peak. Due to the overestimated wind speed and the simulated wind direction not completely veering to the east as observations (about 100° in Figure 10b), the model failed to predict the timing and the magnitude of the O_3 peaks caused by the second plume. The process analysis on this day over the Gulf of Mexico (black box in Figure 2) shows ADV, in addition to CHEM, contributes to the enhanced O_3

315   levels at 10:00 and 13:00 (Figure S9), which respectively corresponds to the two plumes under northerly and

316   easterly winds and highlights the importance of regional transport. This also demonstrates that the contributions

317   from ADV to the increase of O_3 can be high on some specific cases, which can be averaged out in our composite

318   analysis of Figure 5.

319
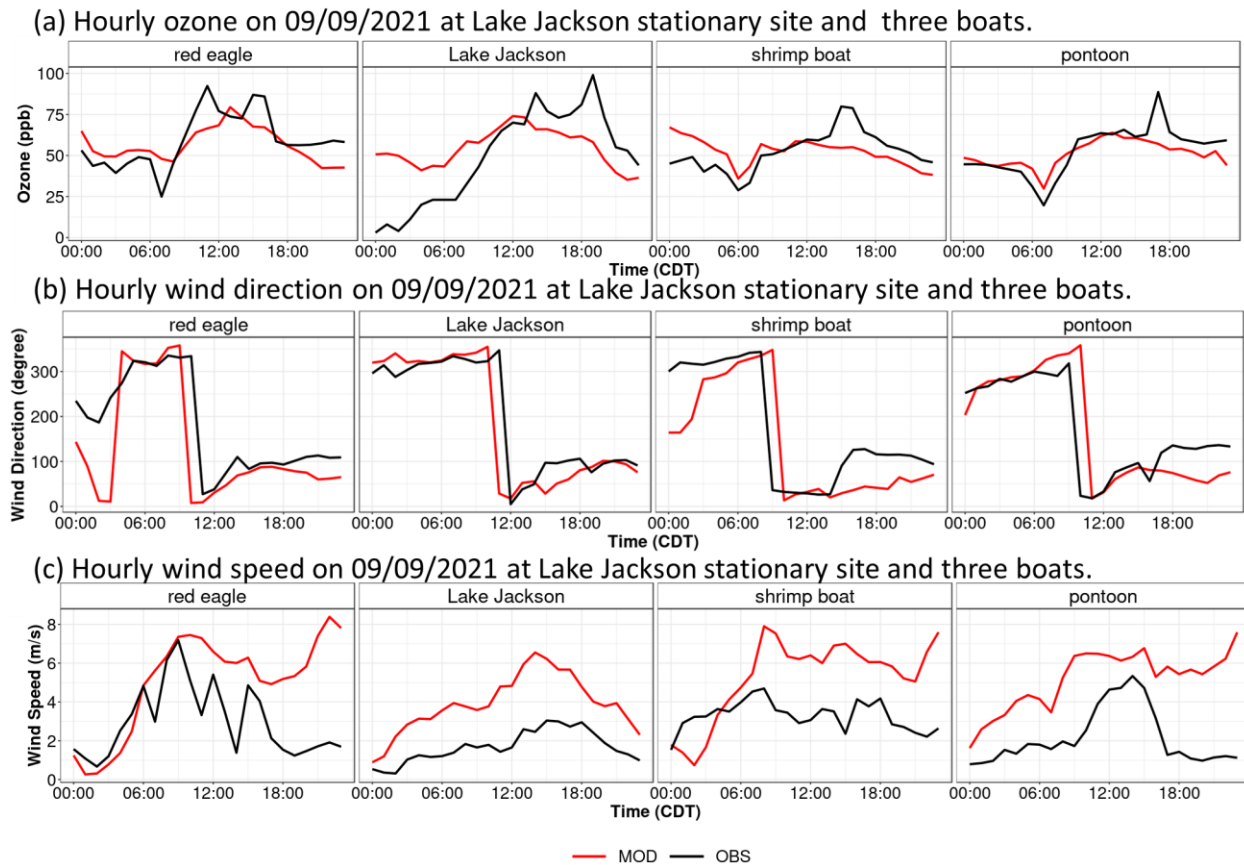
320

321   **Figure 10. Hourly ozone (a), wind direction (b), and wind speed (c) on September 9 from observations at the Lake Jackson**
322   **CAMS site (square mark in Figure 8) and three boats (black) in comparison with model simulations (red).**

323

324   In summary, the wind direction changes from the north to the east on September 9 caused two O_3 peaks, as captured

325   by the Red Eagle boat and the Lake Jackson site. This corresponds to the two simulated ozone plumes shown in the

326   maps. One plume is produced locally and the other is transported from the eastern boundary of the domain. The

327   model overestimates the wind speed, and the simulated wind direction does not change entirely to easterly, leading

328   to lower or totally missed and temporally mismatched O_3 peaks relative to observations.

3.3.2 Case study of October 7, 2021
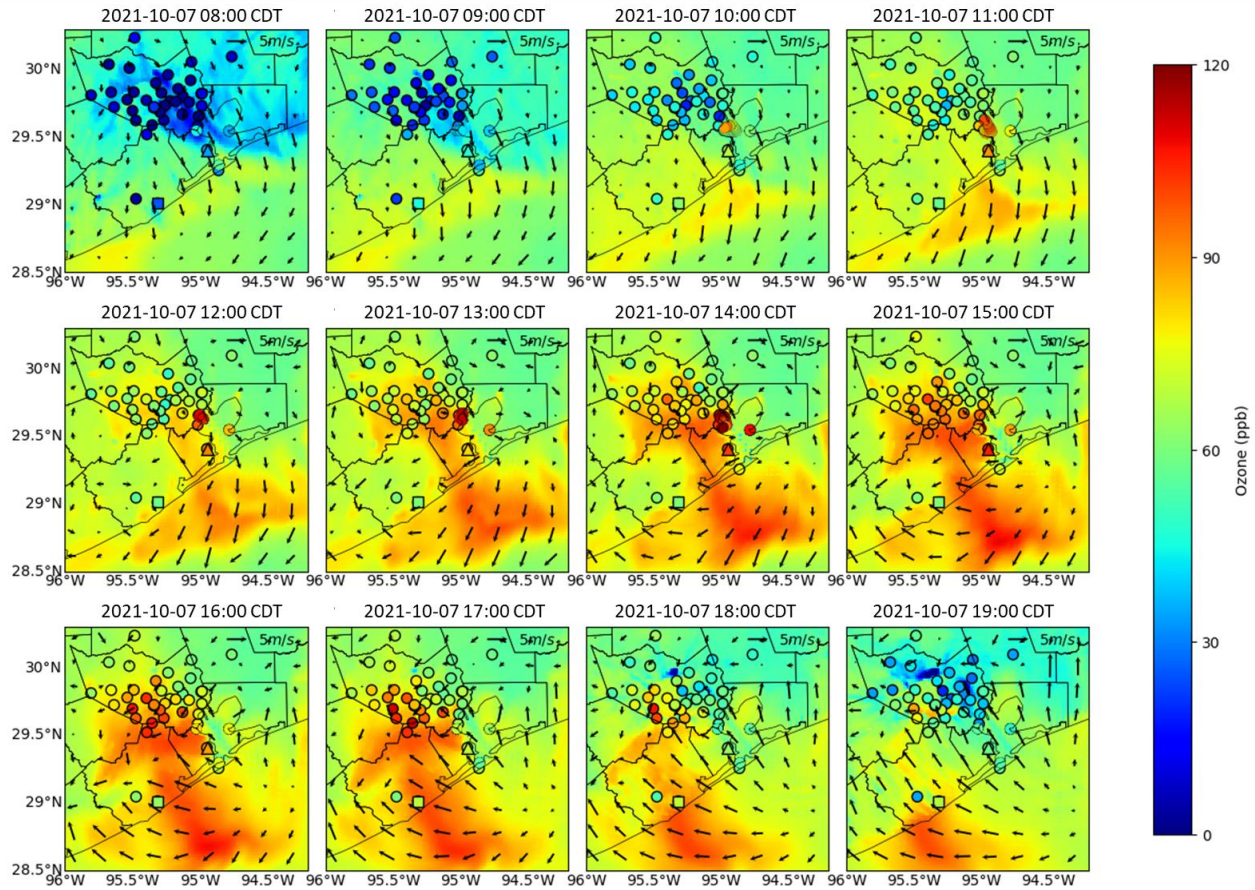
Figure 11. Same as Figure 8 but on October 7 with the square and triangle marks representing the Oyster Creek and Texas City CAMS sites, respectively.

On October 7, the pontoon boat observed the highest one-minute O_3 concentration (135 ppb) throughout the entire campaign period. This day started with weak northwesterly winds in the morning under post-frontal conditions, leading to high O_3 concentrations along the Gulf coast (Figure 11). The winds transitioned to northeasterly near 11:00 (Figure 12b), marking the onset of the Galveston Bay breeze at the pontoon and shrimp boat and the Texas City site (triangle label in Figure 11) and the Gulf breeze at the Oyster Creek site (square label in Figure 11), both accompanied by an increase of O_3 (Figure 12a) and wind speed (Figure 12c). By contrast, the model predicted a late onset of the Bay/Gulf breezes by two to three hours with a generally higher wind speed than was observed. Afterward, the wind directions further shifted to the east to southeast between 14:00 to 18:00 as the Gulf breezes propagated to all four locations in Figure 12b, causing the highest O_3 mixing ratios therein. Similarly, the model overestimated the Gulf breeze intensity, leading to the underestimation of O_3 at the three locations along Galveston Bay. The model also continuously overestimated the moderate level of O_3 (60-70 ppb) at the Oyster Creek site under the Gulf breeze from 11:00 to 20:00, implying that the lifetime of O_3 or its precursors over water was likely overpredicted. Different from September 9, the process analysis on this local-scale event indicates CHEM is the major process leading to high O_3 concentrations over the Gulf of Mexico (Figure S10). ADV only contributes to the

347 increase of O_3 at 08:00-09:00, corresponding to the offshore transport of O_3 in the morning under northwesterly
348 winds.

349
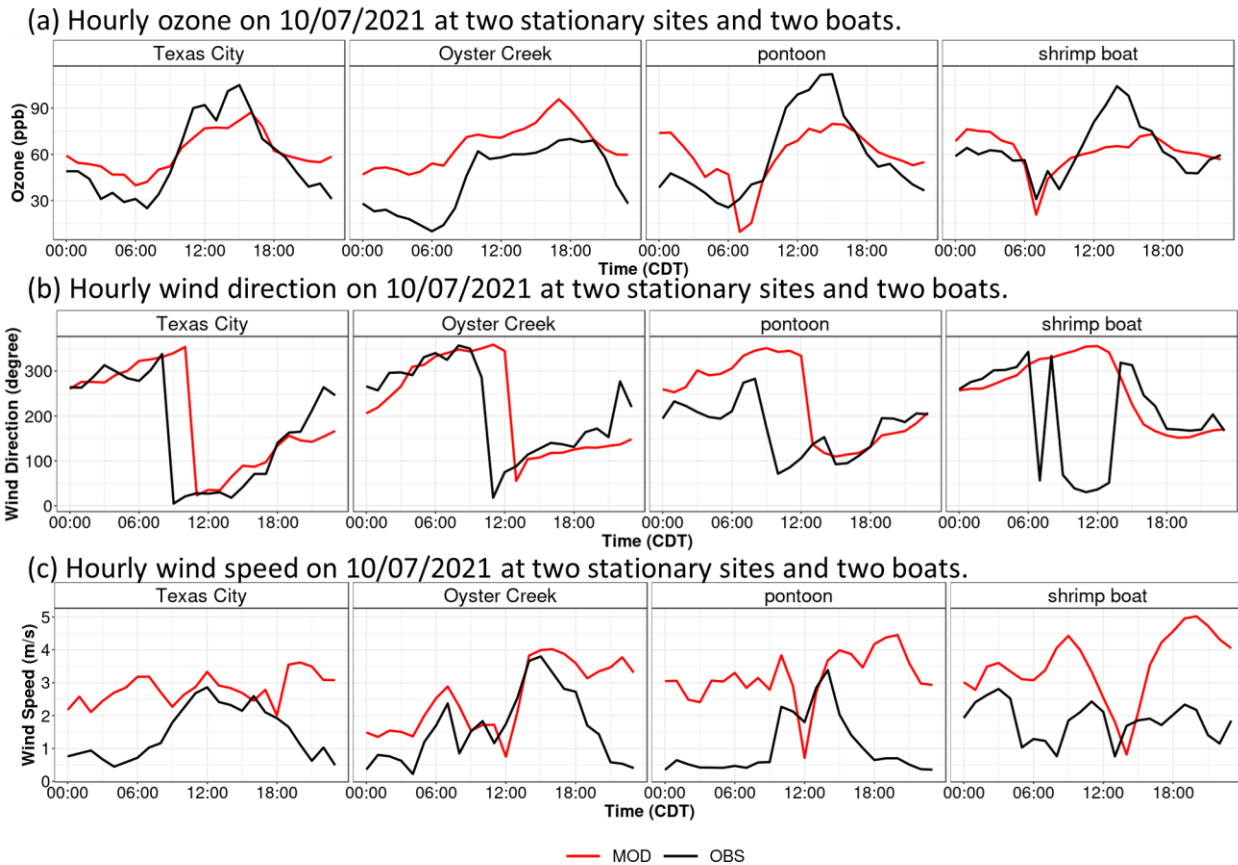
Figure 12. Same as Figure 10 but on October 7 with the Texas City (triangle mark in Figure 11) and Oyster Creek (square mark in Figure 11) CAMS sites and two boats.

352

353 To sum up, the high O_3 event on October 7 was related to the mesoscale Galveston Bay and Gulf breeze
354 recirculation. Two boats and the Texas City site captured the start of the Bay breeze at ~11:00 and the development
355 of the Gulf breeze at 14:00 – 18:00, the latter of which leads to peak hourly O_3 by bringing the aged O_3 and
356 emissions back to land. Affected continuously by the Gulf breeze from 11:00 to 20:00, O_3 at the Oyster Creek site
357 stayed at 60 – 70 ppb. The model predicts the onset of the Bay and Gulf breezes two to three hours late with higher
358 wind speed, causing the delayed and lower O_3 peaks along Galveston Bay.

359 **4 Conclusions**

360 As part of the TRACER-AQ 2021 field campaign in the Houston area, three boats, a UH pontoon boat and two
361 commercial vessels, equipped with an automatic sampling system and ozonesonde launches were deployed in
362 Galveston Bay and the Gulf of Mexico from July to October. The resulting datasets, including the surface and

363 vertical O_3 concentrations and various meteorological parameters, provide a unique opportunity to evaluate the

364 performance of TCEQ's regulatory WRF-CAMx modeling system regarding its ability to capture the high offshore

365 O_3 events. Driven by the optimized WRF meteorological outputs, the CAMx model can satisfactorily capture the

366 spatiotemporal variability of daytime O_3 for the three boats ($R > 0.70$) with an overall $4 - 8$ ppb ($9\% - 22\%$)

367 overestimation mainly caused by the high positive biases on clean days. During high-O_3 events, the model tends to

368 underestimate O_3 by 5 ppb near the surface and by 10 ppb up to 4 km aloft.

369 The reasonable model performance provides credibility for relying on the model's process analysis tool to

370 investigate the factors responsible for the high-O_3 episodes over the Gulf of Mexico. The results show that O_3

371 chemistry is the major process leading to high O_3 concentrations relative to clean conditions. A region-wide increase

372 of long-lived VOC species through advection, such as paraffin, formaldehyde, and acetaldehyde, accelerated O_3

373 production rates under a NO_x-limited regime. In the meantime, the enhanced VOCs can produce more O_3 near

374 western Galveston Bay and off the Gulf coast under high-NO_x concentrations brought by the northeasterly winds

375 from the Houston Ship Channel. Thus, the higher O_3 chemical production over water can be from both NOx- and

376 VOC-limited regimes.

377 Two cases, September 9 and October 7, were then selected to illustrate the development of high-O_3 events further.

378 Both cases involved north/northeast morning winds transporting the inland emissions toward the sea, shifting to the

379 east/southeast in the afternoon, and transporting the offshore O_3 and its precursors to the land. Therefore, well-

380 represented wind conditions are of great importance for air quality models to accurately capture the timing and

381 magnitude of elevated O_3 levels in these cases. However, the two cases differ in terms of atmospheric scale. The

382 event on September 9 was influenced by a large-scale circulation with regionally homogeneous wind conditions.

383 The easterly winds in the afternoon brought a second air plume from the eastern boundary of the domain following

384 the first locally produced plume, illustrating the contributions of regional advection, in addition to chemistry, to the

385 high O_3 mixing ratios in this case. Conversely, the October 7 case was dominated by the mesoscale development of

386 Bay and Gulf breezes, characterized by a generally lower wind speed and higher O_3 level. Double O_3 peaks can also

387 be observed near Galveston Bay, such as the Texas City site in this case, corresponding to the arrival of the Bay and

388 Gulf breezes, respectively. The model mispredicted the timing of the wind direction shift and overestimated the

389 wind speed in both cases, leading to the temporally mismatched and numerically buffered O_3 peaks.

390 This study reveals the important role of chemical O_3 production over Galveston Bay and the Gulf of Mexico from

391 precursors emitted from adjacent land and the Ship Channel or transported regionally from the northeastern states.

392 The high O_3 produced offshore can then be transported back to land and cause O_3 exceedances at the air quality

393 monitors. Therefore, local and regional emissions need to be stringently regulated to reduce the frequency of such

394 events. Additionally, wind conditions are critical meteorological factors leading to these high-O_3 episodes and thus

395 need to be well represented in photochemical models to have an accurate air quality forecast in urban coastal

396 regions.

Acknowledgments

This research was supported by the Texas Commission for Environmental Quality (TCEQ, Grant Numbers 582-22-31544-019) and the State of Texas Air Quality Research Program (AQRP, Project 20-008). The findings, opinions, and conclusions are the work of the author(s) and do not necessarily represent the findings, opinions, or conclusions of the TCEQ or AQRP. We acknowledge the individuals and groups who collected and shared the TRACER-AQ 2021 filed campaign datasets.

Data Availability

CAMx and WRF models are publicly available at https://www.camx.com/ (last access: 22 September 2023) and https://www2.mmm.ucar.edu/wrf/users/download/get_source.html (last access: 22 September 2023), respectively. CAMS data can be downloaded from the TAMIS web interface (https://www17.tceq.texas.gov/tamis/index.cfm?fuseaction=home.welcome, last access: 22 September 2023), and other campaign data is archived in the TRACER-AQ website (https://www-air.larc.nasa.gov/cgi-bin/ArcView/traceraq.2021, last access: 22 September 2023).

Competing interests

The authors declare that they have no conflict of interest.

Author contributions

YW conceived the research idea. WL, XL and ES conducted the model simulation. TG, JF and PW provided the field observations. WL performed the data analysis and drafted the initial manuscript. All authors contributed to the interpretation of the results and the preparation of the manuscript.

References

Abdi-Oskouei, M., Carmichael, G., Christiansen, M., Ferrada, G., Roozitalab, B., Sobhani, N., Wade, K., Czarnetzki, A., Pierce, R. B., Wagner, T., and Stanier, C.: Sensitivity of Meteorological Skill to Selection of WRF-Chem Physical Parameterizations and Impact on Ozone Prediction During the Lake Michigan Ozone Study (LMOS), J. Geophys. Res. Atmospheres, 125, e2019JD031971, https://doi.org/10.1029/2019JD031971, 2020.

Abdi-Oskouei, M., Roozitalab, B., Stanier, C. O., Christiansen, M., Pfister, G., Pierce, R. B., McDonald, B. C., Adelman, Z., Janseen, M., Dickens, A. F., and Carmichael, G. R.: The Impact of Volatile Chemical Products, Other VOCs, and NOx on Peak Ozone in the Lake Michigan Region, J. Geophys. Res. Atmospheres, 127, e2022JD037042, https://doi.org/10.1029/2022JD037042, 2022.

Baker, K. R., Liljegren, J., Valin, L., Judd, L., Szykman, J., Millet, D. B., Czarnetzki, A., Whitehill, A., Murphy, B., and Stanier, C.: Photochemical model representation of ozone and precursors during the 2017 Lake Michigan ozone study (LMOS), Atmos. Environ., 293, 119465, https://doi.org/10.1016/j.atmosenv.2022.119465, 2023.

Banta, R. M., Senff, C. J., Nielsen-Gammon, J., Darby, L. S., Ryerson, T. B., Alvarez, R. J., Sandberg, S. P., Williams, E. J., and Trainer, M.: A Bad Air Day in Houston, Bull. Am. Meteorol. Soc., 86, 657–670, https://doi.org/10.1175/BAMS-86-5-657, 2005.

431   Bernier, C., Wang, Y., Gronoff, G., Berkoff, T., Knowland, K. E., Sullivan, J. T., Delgado, R., Caicedo, V., and
432   Carroll, B.: Cluster-based characterization of multi-dimensional tropospheric ozone variability in coastal regions: an
433   analysis of lidar measurements and model results, Atmospheric Chem. Phys., 22, 15313–15331,
434   https://doi.org/10.5194/acp-22-15313-2022, 2022.

435   Burkholder, J. B., Sander, S. P., Abbatt, J. P. D. A. D., Barker, J. R., Huie, R. E., Kolb, C. E., Iii, M. J. K., Orkin, V.
436   L., Wilmouth, D. M., and Wine, P. H.: Chemical Kinetics and Photochemical Data for Use in Atmospheric Studies:
437   Evaluation number 18, JPL Publ. 15-10, Jet Propulsion Laboratory, Pasadena, CA, 2019.

438   Caicedo, V., Rappenglueck, B., Cuchiara, G., Flynn, J., Ferrare, R., Scarino, A. J., Berkoff, T., Senff, C., Langford,
439   A., and Lefer, B.: Bay Breeze and Sea Breeze Circulation Impacts on the Planetary Boundary Layer and Air Quality
440   From an Observed and Modeled DISCOVER-AQ Texas Case Study, J. Geophys. Res. Atmospheres, 124, 7359–
441   7378, https://doi.org/10.1029/2019JD030523, 2019.

442   Chen, F. and Dudhia, J.: Coupling an Advanced Land Surface–Hydrology Model with the Penn State–NCAR MM5
443   Modeling System. Part I: Model Implementation and Sensitivity, Mon. Weather Rev., 129, 569–585,
444   https://doi.org/10.1175/1520-0493(2001)129<0569:CAALSH>2.0.CO;2, 2001.

445   Dacic, N., Sullivan, J. T., Knowland, K. E., Wolfe, G. M., Oman, L. D., Berkoff, T. A., and Gronoff, G. P.:
446   Evaluation of NASA's high-resolution global composition simulations: Understanding a pollution event in the
447   Chesapeake Bay during the summer 2017 OWLETS campaign, Atmos. Environ., 222, 117133,
448   https://doi.org/10.1016/j.atmosenv.2019.117133, 2020.

449   Darby, L. S.: Cluster Analysis of Surface Winds in Houston, Texas, and the Impact of Wind Patterns on Ozone, J.
450   Appl. Meteorol. Climatol., 44, 1788–1806, https://doi.org/10.1175/JAM2320.1, 2005.

451   Dreessen, J., Orozco, D., Boyle, J., Szymborski, J., Lee, P., Flores, A., and Sakai, R. K.: Observed ozone over the
452   Chesapeake Bay land-water interface: The Hart-Miller Island Pilot Project, J. Air Waste Manag. Assoc., 69, 1312–
453   1330, https://doi.org/10.1080/10962247.2019.1668497, 2019.

454   Dreessen, J., Ren, X., Gardner, D., Green, K., Stratton, P., Sullivan, J. T., Delgado, R., Dickerson, R. R., Woodman,
455   M., Berkoff, T., Gronoff, G., and Ring, A.: VOC and trace gas measurements and ozone chemistry over the
456   Chesapeake Bay during OWLETS-2, 2018, J. Air Waste Manag. Assoc., 73, 178–199,
457   https://doi.org/10.1080/10962247.2022.2136782, 2023.

458   Dye, T. S., Roberts, P. T., and Korc, M. E.: Observations of Transport Processes for Ozone and Ozone Precursors
459   during the 1991 Lake Michigan Ozone Study, J. Appl. Meteorol. Climatol., 34, 1877–1889,
460   https://doi.org/10.1175/1520-0450(1995)034<1877:OOTPFO>2.0.CO;2, 1995.

461   Nonattainment Areas for Criteria Pollutants (Green Book): https://www.epa.gov/green-book, last access: 6 January
462   2023.

463   Foken, T.: 50 Years of the Monin–Obukhov Similarity Theory, Bound.-Layer Meteorol., 119, 431–447,
464   https://doi.org/10.1007/s10546-006-9048-6, 2006.

465   Goldberg, D. L., Loughner, C. P., Tzortziou, M., Stehr, J. W., Pickering, K. E., Marufu, L. T., and Dickerson, R. R.:
466   Higher surface ozone concentrations over the Chesapeake Bay than over the adjacent land: Observations and models
467   from the DISCOVER-AQ and CBODAQ campaigns, Atmos. Environ., 84, 9–19,
468   https://doi.org/10.1016/j.atmosenv.2013.11.008, 2014.

469   Griggs, T., Flynn, J., Wang, Y., Alvarez, S., Comas, M., and Walter, P.: Characterizing Over-Water High Ozone
470   Events in the Houston-Galveston-Brazoria Region During July-October 2021, Bull. Am. Meteorol. Soc., submitted.

471 Iacono, M. J., Delamere, J. S., Mlawer, E. J., Shephard, M. W., Clough, S. A., and Collins, W. D.: Radiative forcing
472 by long-lived greenhouse gases: Calculations with the AER radiative transfer models, J. Geophys. Res.
473 Atmospheres, 113, https://doi.org/10.1029/2008JD009944, 2008.

474 Kommalapati, R. R., Liang, Z., and Huque, Z.: Photochemical model simulations of air quality for Houston–
475 Galveston–Brazoria area and analysis of ozone–NOx–hydrocarbon sensitivity, Int. J. Environ. Sci. Technol., 13,
476 209–220, https://doi.org/10.1007/s13762-015-0862-6, 2016.

477 Leuchner, M. and Rappenglück, B.: VOC source–receptor relationships in Houston during TexAQS-II, Atmos.
478 Environ., 44, 4056–4067, https://doi.org/10.1016/j.atmosenv.2009.02.029, 2010.

479 Li, W., Wang, Y., Bernier, C., and Estes, M.: Identification of Sea Breeze Recirculation and Its Effects on Ozone in
480 Houston, TX, During DISCOVER-AQ 2013, J. Geophys. Res. Atmospheres, 125, e2020JD033165,
481 https://doi.org/10.1029/2020JD033165, 2020.

482 Li, X. and Rappenglück, B.: A WRF–CMAQ study on spring time vertical ozone structure in Southeast Texas,
483 Atmos. Environ., 97, 363–385, https://doi.org/10.1016/j.atmosenv.2014.08.036, 2014.

484 Liu, X., Wang, Y., Wasti, S., Li, W., Soleimanian, E., Flynn, J., Griggs, T., Alvarez, S., Sullivan, J. T., Roots, M.,
485 Twigg, L., Gronoff, G., Berkoff, T., Walter, P., Estes, M., Hair, J. W., Shingler, T., Scarino, A. J., Fenn, M., and
486 Judd, L.: Evaluating WRF-GC v2.0 predictions of boundary layer and vertical ozone profiles during the 2021
487 TRACER-AQ campaign in Houston, Texas, EGUsphere, 1–33, https://doi.org/10.5194/egusphere-2023-892, 2023.

488 Mazzuca, G. M., Ren, X., Loughner, C. P., Estes, M., Crawford, J. H., Pickering, K. E., Weinheimer, A. J., and
489 Dickerson, R. R.: Ozone production and its sensitivity to NO_x and VOCs: results from the DISCOVER-AQ field
490 experiment, Houston 2013, Atmospheric Chem. Phys., 16, 14463–14474, https://doi.org/10.5194/acp-16-14463-
491 2016, 2016.

492 Misenis, C. and Zhang, Y.: An examination of sensitivity of WRF/Chem predictions to physical parameterizations,
493 horizontal grid spacing, and nesting options, Atmospheric Res., 97, 315–334,
494 https://doi.org/10.1016/j.atmosres.2010.04.005, 2010.

495 Morrison, H., Thompson, G., and Tatarskii, V.: Impact of Cloud Microphysics on the Development of Trailing
496 Stratiform Precipitation in a Simulated Squall Line: Comparison of One- and Two-Moment Schemes, Mon. Weather
497 Rev., 137, 991–1007, https://doi.org/10.1175/2008MWR2556.1, 2009.

498 Nakanishi, M. and Niino, H.: Development of an Improved Turbulence Closure Model for the Atmospheric
499 Boundary Layer, J. Meteorol. Soc. Jpn. Ser II, 87, 895–912, https://doi.org/10.2151/jmsj.87.895, 2009.

500 Ngan, F. and Byun, D.: Classification of Weather Patterns and Associated Trajectories of High-Ozone Episodes in
501 the Houston–Galveston–Brazoria Area during the 2005/06 TexAQS-II, J. Appl. Meteorol. Climatol., 50, 485–499,
502 https://doi.org/10.1175/2010JAMC2483.1, 2011.

503 Pan, S., Choi, Y., Roy, A., Li, X., Jeon, W., and Souri, A. H.: Modeling the uncertainty of several VOC and its
504 impact on simulated VOC and ozone in Houston, Texas, Atmos. Environ., 120, 404–416,
505 https://doi.org/10.1016/j.atmosenv.2015.09.029, 2015.

506 Pan, S., Choi, Y., Roy, A., and Jeon, W.: Allocating emissions to 4 km and 1 km horizontal spatial resolutions and
507 its impact on simulated NOx and O3 in Houston, TX, Atmos. Environ., 164, 398–415,
508 https://doi.org/10.1016/j.atmosenv.2017.06.026, 2017.

509 Rappenglück, B., Perna, R., Zhong, S., and Morris, G. A.: An analysis of the vertical structure of the atmosphere and
510 the upper-level meteorology and their impact on surface ozone levels in Houston, Texas, J. Geophys. Res.
511 Atmospheres, 113, https://doi.org/10.1029/2007JD009745, 2008.

512   Sillman, S.: The use of NO y , H2O2, and HNO3 as indicators for ozone-NO x -hydrocarbon sensitivity in urban
513   locations, J. Geophys. Res. Atmospheres, 100, 14175–14188, https://doi.org/10.1029/94JD02953, 1995.

514   Soleimanian, E., Wang, Y., and Estes, M.: Long-term trend in surface ozone in Houston-Galveston-Brazoria:
515   Sectoral contributions based on changes in volatile organic compounds, Environ. Pollut., 308, 119647,
516   https://doi.org/10.1016/j.envpol.2022.119647, 2022.

517   Soleimanian, E., Wang, Y., Li, W., Liu, X., Griggs, T., Flynn, J., Walter, P. J., and Estes, M. J.: Understanding
518   ozone episodes during the TRACER-AQ campaign in Houston, Texas: The role of transport and ozone production
519   sensitivity to precursors, Sci. Total Environ., 900, 165881, https://doi.org/10.1016/j.scitotenv.2023.165881, 2023.

520   Sullivan, J. T., Berkoff, T., Gronoff, G., Knepp, T., Pippin, M., Allen, D., Twigg, L., Swap, R., Tzortziou, M.,
521   Thompson, A. M., Stauffer, R. M., Wolfe, G. M., Flynn, J., Pusede, S. E., Judd, L. M., Moore, W., Baker, B. D., Al-
522   Saadi, J., and McGee, T. J.: The Ozone Water–Land Environmental Transition Study: An Innovative Strategy for
523   Understanding Chesapeake Bay Pollution Events, Bull. Am. Meteorol. Soc., 100, 291–306,
524   https://doi.org/10.1175/BAMS-D-18-0025.1, 2019.

525   Wesely, M. L.: Parameterization of surface resistances to gaseous dry deposition in regional-scale numerical
526   models, Atmos. Environ., 41, 52–63, https://doi.org/10.1016/j.atmosenv.2007.10.058, 1989.

527   Xiao, X., Cohan, D. S., Byun, D. W., and Ngan, F.: Highly nonlinear ozone formation in the Houston region and
528   implications for emission controls, J. Geophys. Res. Atmospheres, 115, https://doi.org/10.1029/2010JD014435,
529   2010.

530   Yu, S., Mathur, R., Pleim, J., Pouliot, G., Wong, D., Eder, B., Schere, K., Gilliam, R., and Trivikrama Rao, S.:
531   Comparative evaluation of the impact of WRF–NMM and WRF–ARW meteorology on CMAQ simulations for O3
532   and related species during the 2006 TexAQS/GoMACCS campaign, Atmospheric Pollut. Res., 3, 149–162,
533   https://doi.org/10.5094/APR.2012.015, 2012.

534   Zhang, C., Wang, Y., and Hamilton, K.: Improved Representation of Boundary Layer Clouds over the Southeast
535   Pacific in ARW-WRF Using a Modified Tiedtke Cumulus Parameterization Scheme, Mon. Weather Rev., 139,
536   3489–3513, https://doi.org/10.1175/MWR-D-10-05091.1, 2011.

537